International Journal of Bifurcation and Chaos, Vol. 24, No. 10 (2014) 1430029 (23 pages)

DOI: 10.1142/S0218127414300298

Geometry of Basins of Attraction and Heteroclinic Connections in Coupled Bistable Systems

Daniel Lyons, Joseph M. Mahaffy, Sara Wang and Antonio Palacios*
Nonlinear Dynamical Systems Group, Department of Mathematics, San Diego State University, San Diego, CA 92182, USA
**palacios@euler.sdsu.edu*

Visarath In
Space and Naval Warfare Systems Center Pacific, Code 71730, 53560 Hull Street, San Diego, CA 92152-5001, USA
visarath@spawar.navy.mil

Received April 29, 2014

The fundamental principle of bistability is widely used across various disciplines, including biology, chemistry, mechanics, physics, electronics and materials science. As the need for more powerful, efficient and sensitive complex-engineered systems grow, networks of coupled bistable systems have gained significant attention in recent years. Modeling and analysis of such higher-dimensional systems is usually focused on finding conditions for the existence and stability of typical invariant sets, i.e. steady states, periodic solutions and chaotic sets. High-dimensionality leads to complex patterns of collective behavior. Which type of behavior is exhibited by a network depends greatly on the initial conditions. Thus, it is also important to study the geometric structure and evolution of the basins of attraction of such patterns. In this manuscript, a complete study of the basins of attraction of a ring of bistable systems, coupled unidirectionally, is presented. 3D visualizations are included to aid the discussion of the changes in the basins of attraction as the coupling parameter varies. The results are broad enough that they can be applied to a wide range of systems with similar coupling topologies.

Keywords: Basins of attraction; stable manifold theorem; bifurcations.

1. Introduction

Bistability — the property that allows a system to rest in either of two states — underlies the basic behavior of many natural and artificial systems. States may include typical invariant sets, such as equilibrium points, periodic and quasi-periodic solutions, and chaotic attractors. In the absence of an external stimulus, the state variable of a bistable system will relax to one of the invariant sets, and it will remain in that state unless it is switched or forced to another state. It is in this sense that the system exhibits "memory". Which invariant set the system will relax to depends typically on the set of initial conditions. All bistable systems employ some form of energy source, either through external forcing or through the coupling mechanism, as the underlying principle that allows them to switch between states. Here the focus is on the coupling mechanism since that is the structure for building many of the novel, ultra-sensitive sensors.

In biological systems, bistability is a key feature for understanding and engineering cellular functions such as: storing and processing information by the human brain during the decision-making process [Ajo-Franklin *et al.*, 2007]; regulation of the cell cycle [Tyson *et al.*, 2001; Solomon, 2003]; sporulation, which controls the timing and dynamics of dramatic responses to stress [Voigt *et al.*, 2005];

design and construction of synthetic toggle switches [Gardner *et al.*, 2000]; and in gene regulatory networks responsible for embryonic stem cell fate decisions [Chickarmane *et al.*, 2006]. In chemical systems bistability is central to the analysis of relaxation kinetics [Wilhelm, 2009]. In mechanical systems, bistable mechanisms are commonly employed in the design and fabrications of Micro-Electro-Mechanical-Systems (MEMS) versions of relays, valves, clips and threshold switches [Qiu & Lang, 2004; Hoffmann *et al.*, 1999]. In electronics, hysteresis and bistability are combined to design and fabricate Schmitt trigger circuits, which convert analog input signals to digital output signals [Schmitt, 1938]. In neuroscience, bistability is at the core of Hopfield models [Cohen & Grossberg, 1983; Hopfield, 1982, 1984], which describe the input/output response of neurons through differential equations of the form

$$\tau_i \frac{dV_i}{dt} = -V_i + g(V_i), \tag{1}$$

where τ_i is a suitable time constant that controls how quickly unit(neuron) i responds to a stimulus, V_i is the output (typically voltage) of unit i, and g is the activation function, which normally represents a saturation nonlinearity property of neurons.

Nowadays, Eq. (1) serves as the basis of the modern theory of neural-computation and neural networks. However, there is also a close analogy between the Hopfield model, Eq. (1), and the model equation of ferromagnetic materials. That is, the magnetization state or magnetic spin of a hysteretic ferromagnetic core (treated as a macroscopic single-domain entity via mean field approximation [Tome & De Oliveira, 1990]), subject to an externally applied field $h(t)$, can switch between two bistable states, up or down. The switching is regulated through a nonlinear activation function with a saturation nonlinearity, just as a neuron responds to stimuli. Thus, magnetic spins behave like neurons. Indeed, both systems are governed by the same type of equation

$$\tau_i \dot{x}_i = -x_i + \tanh(c(x_i + h(t))), \tag{2}$$

where x_i represents the magnetic spin state in a ferromagnetic sample i with the saturation nonlinearity $g(x_i) = \tanh(c\,x_i)$, in which c is a temperature- and material-dependent parameter governing bistability. The system is bistable for $c \geq 1$. The external field $h(t)$ is typically a periodic forcing function such as a square, sinusoidal, or triangle wave. In recent years, this analogy has been exploited to model, analyze, design, and fabricate a new generation of ultra-sensitive sensor systems for detecting and measuring magnetic as well as electric fields [In *et al.*, 2003; Bulsara *et al.*, 2004]. The new technology takes advantage of a more robust property of positive feedback loops, albeit less employed in engineered systems, and sensitivity amplification [Goldbeter & Koshland, 1981]. More specifically, it has been demonstrated, theoretically and experimentally, that coupling an *odd* number of over-damped bistable ferromagnetic cores, with unidirectional positive feedback, can lead to a branch of globally asymptotically stable oscillations. These oscillations emerge via heteroclinic connections between the multiple equilibrium states that are created by the symmetry of the topology. Near the point of bifurcation of the heteroclinic cycle, the ensuing oscillations are highly sensitive to symmetry breaking effects that occur when an external signal ε is present. This sensitivity amplification mechanism renders the coupled bistable system ultra-sensitive to detect and measure external signals. The governing equations can be rewritten in the following form

$$\tau_i \dot{x}_i = -x_i + \tanh(c(x_i + \lambda x_{i+1} + \varepsilon)), \tag{3}$$

where λ is the coupling positive feedback parameter and $i = 1, \ldots, N \mod N$. Observe that the external forcing function $h(t)$ has been replaced by the positive feedback term λx_{i+1} because the oscillations are now induced by the coupling topology, which is another desirable property of positive feedback and a novelty of the design.

Most works on bistable systems, single and networks, focus on determining the conditions for the existence and bifurcations of typical invariant sets, i.e. equilibria, periodic solutions and chaos. Since the qualitative behavior of the long-term motion of a given system can vary dramatically depending on the location of the basin of attraction of the initial condition, it is also important to investigate the structure and changes for the basins of those invariant sets. In the case of networks of coupled bistable systems, the interconnection of multiple units leads to high-dimensional nonlinear systems with possible complex patterns of collective behavior, such as heteroclinic connections. Visualizing the basins of attraction of this and other collective patterns is critical to develop a more comprehensive

understanding of networks. In this work, we explore the geometric structure and evolution of the basins of attraction of a coupled bistable system. We provide detailed descriptions of the changes in the basins of attractions with 3D figures. We also provide details for generating the graphic pictures for the basins of attraction. As a test bed, we consider the Hopfield model equations or, equivalently, the coupled ferromagnetic model (3). Our results depend strongly on the nature of the many equilibria in this system and on applying the Stable Manifold Theorem from differential equations [Teschl, 2012; Wiggins, 1990]. However, we wish to emphasize that our techniques can be readily extended to study other related networks of coupled bistable systems.

The manuscript is organized as follows. In Sec. 2, we provide a brief overview of the bifurcation diagram that captures the changes of behavior in the model equations (3) as the coupling parameter λ, i.e. strength of positive feedback, is varied. Then in Sec. 3, a detailed description of the transitions in the dynamics and the evolution and 3D visualization of the corresponding basins of attraction is presented. The description is organized into eight regions or intervals of coupling strength. In Sec. 4, the techniques used to construct and visualize the basins of attraction are discussed. More technical details are included in the Appendices. Section 5 contains a summary and discussion of our results.

2. Geometric Description: A Brief Overview

This paper concentrates on the 3D visualization of the basins of attraction for a coupled bistable system of the form defined by Eq. (3). We start with a brief description of the solution sets for this system and a brief discussion of how their basins of attraction evolve as the coupling strength λ varies. The bifurcation methods generalize to arbitrary N, but the detailed specifics for finding and visualizing the basins of attraction are limited to 3D, so we focus on $N = 3$. The qualitative behavior of Eq. (3) for larger N with N odd is similar to our results below, but visualizing basins of attraction would be difficult. When N is even, heteroclinic connections do not exist [In *et al.*, 2003] nor do periodic oscillations — only equilibrium solutions. Without loss of generality, the external field ε is set to zero and after rescaling time, the time constant can be set to $\tau_i = 1$. The specific system of equations used for our subsequent figures satisfies:

$$\begin{aligned}\dot{x}_1 &= -x_1 + \tanh(c(x_1 + \lambda x_2))\\ \dot{x}_2 &= -x_2 + \tanh(c(x_2 + \lambda x_3))\\ \dot{x}_3 &= -x_3 + \tanh(c(x_3 + \lambda x_1)),\end{aligned} \tag{4}$$

where $c = 3$. Observe now that since the activation function tanh is odd, Eq. (4) remains unchanged under the transformation $x_i \mapsto \pm x_i$. Under unidirectional coupling with positive feedback the network equations are also unchanged under the cyclic transformation $x_i \mapsto x_{i+1}$. It follows that the symmetries of the coupled bistable system (4) are captured by the 24-elements group $\Gamma \simeq \mathbf{Z}_2^3 \otimes \mathbf{Z}_3$, which is generated by

$$\begin{aligned}(x_1, x_2, x_3) &\mapsto (\pm x_1, \pm x_2, \pm x_3)\\ (x_1, x_2, x_3) &\mapsto (x_2, x_3, x_1).\end{aligned}$$

When the coupling parameter is sufficiently large, and negative, then all solutions other than the unstable trivial solution and its 1D symmetric stable manifold, emanating along the line $x_1 = x_2 = x_3$, are attracted to a stable asymmetric periodic orbit with 3-fold symmetry, see Fig. 1. At the

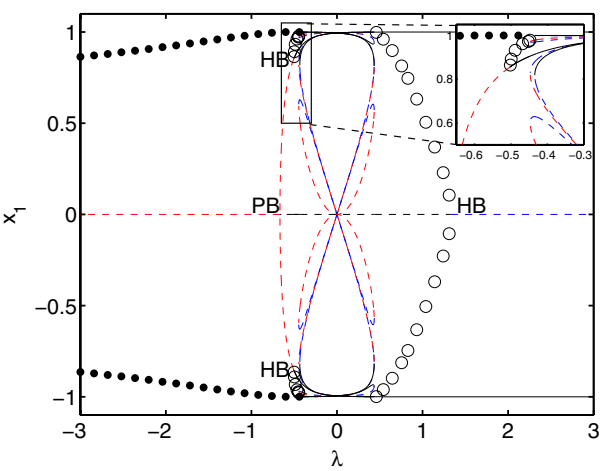

Fig. 1. Bifurcation diagram for System (4) computed in the equilibrium continuation program AUTO [Doedel & Wang, 1994]. The diagram provides the values of x_1 at equilibria and the maximum and minimum values of x_1 at periodic orbits. Solid (dashed) lines indicate stable (unstable) equilibrium points. For unstable equilibria, black (dashed) indicates a 3D unstable manifold, red (dashed) has a 1D stable manifold, and blue (dashed) presents a 2D stable manifold. Filled-in (empty) circles represent stable (unstable) periodic oscillations. Parameters are $c = 3$ and $\epsilon = 0$. Notation: HB denotes Hopf bifurcation points and PB is a pitchfork bifurcation point.

other end, when the coupling parameter is sufficiently large, and positive, then all solutions other than the unstable trivial solution and its 2D stable manifold are attracted to one of two stable symmetric equilibria.

For intermediate values of λ, complex transitions that involve multiple equilibrium points, periodic solutions, and heteroclinic connections are observed. To unravel those transitions we start with a large negative value of λ. As λ increases, there is a pitchfork bifurcation, producing two new symmetric equilibria moving away from the origin along its 1D stable manifold. As λ further increases, the 1D stable manifold expands into two conical regions symmetric about the origin, which morph into two 3-sided pyramidal shaped regions surrounding two symmetric stable equilibria with additional increases in λ. The 3-fold stable limit cycle has its period increase until it spends longer and longer times near six points, which appear as stable equilibria through a saddle node bifurcation. A second saddle node bifurcation produces six other asymmetric equilibria, which arise and generate separatrices. These divide our space into eight basins of attraction. Two are the small symmetric pyramidal shaped regions centered on the line $x_1 = x_2 = x_3$, while the other six attracting regions surround these symmetric regions.

As λ increases to zero, the uncoupled state, these eight basins of attraction shrink or expand until they become simply the eight octants in 3-space with stable equilibria near $x_i \approx \pm 1$ for $i = 1, 2, 3$. As λ becomes more positive, the two symmetric basins of attraction increase in size, while the six asymmetric basins shrink in size. Another saddle node bifurcation occurs with the loss of six stable equilibria in the six asymmetric basins of attraction, and the separatrices between these equilibria and the remaining symmetric equilibria vanish. The remaining 2D stable manifold (separatrix) with 3-fold symmetry divides our 3-space into two basins of attraction containing our only two remaining stable equilibria. Further increases in λ only result in a flattening of this separatrix between the symmetric stable equilibria.

Our methods for visualizing the basins of attraction are a direct consequence of the Stable Manifold Theorem. Basins of attraction for stable equilibria and stable limit cycles are separated by 2D stable manifolds emanating from unstable saddle nodes or unstable limit cycles. Numerically, these manifolds are found by tracking solutions of System (4) backwards in time and triangulating to approximate the complete separatrix. A review of techniques that other authors have employed is available [Krauskopf *et al.*, 2005].

3. Geometry of the Basins of Attraction

We now provide a detailed description of the geometric structure of the basins of attraction described above. The discussion is divided into eight distinct regions or intervals of λ, which are affected by the different bifurcations occurring. We demonstrate that the changes in behavior actually occur via very smooth transitions. The basins of attraction and new equilibria appear or disappear with small and smooth changes, as one expects from a continuous dynamical system.

3.1. *Region I: Small parameter λ*

The discussion begins with the coupling parameter in the range $\lambda < -0.6667$. In this range, there is only the stable limit cycle and the unstable equilibrium at the origin. The unstable equilibrium at the origin has a 1D stable manifold along the line $x_1 = x_2 = x_3$. It follows that any initial condition, except along the line $x_1 = x_2 = x_3$, will asymptotically approach the stable limit cycle similar to the one shown as a black curve in Fig. 2. Numerically, the 1D stable manifold (red line in figure) is easily obtained by starting with points very close to the origin and integrating System (4) backwards in time.

The symmetry of this periodic orbit is critical to the operation of the fluxgate magnetometer. If we define the value $x_1 = 1$ as the first component being ON and $x_1 = -1$ as being OFF with similar definitions for x_2 and x_3, then we see the device cycling in a very regular progression, depending on the order of the coupling. The orbit cycles in a distinct manner, where if the first two components are ON with the third component OFF, then the first component of the device turns OFF. Below we show the natural progress of this device with the negative coupling, where we order the device $\langle x_1, x_2, x_3 \rangle$:

$$\begin{aligned} \langle 1, 1, -1 \rangle &\to \langle -1, 1, -1 \rangle \to \langle -1, 1, 1 \rangle \\ &\to \langle -1, -1, 1 \rangle \to \langle 1, -1, 1 \rangle \\ &\to \langle 1, -1, -1 \rangle. \end{aligned} \tag{5}$$

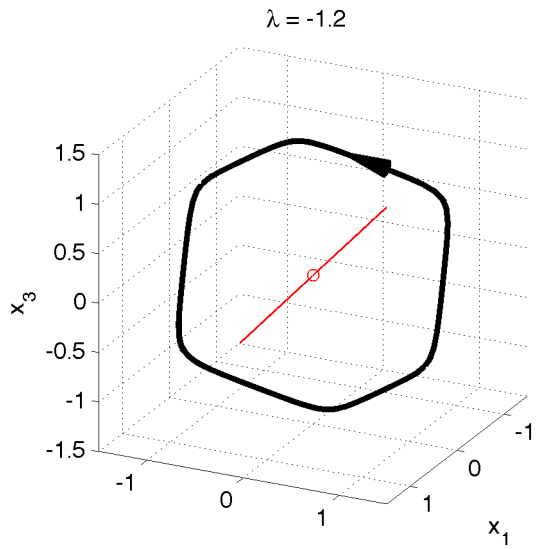

Fig. 2. Basin of attraction for $\lambda = -1.2$. The open red circle represents the unstable equilibrium at the origin, which has a 1D stable manifold along the line $x_1 = x_2 = x_3$. The black closed curve shows the stable limit cycle, which attracts all solutions of System (4), not along the line $x_1 = x_2 = x_3$.

The model simulates this behavior by rapidly moving between the states, then slowing down as the trajectory approaches one of the states above. Figure 3(a) illustrates this behavior showing the rapid transition between the ON and OFF states, then the slowing of the trajectory and a shift of direction as the solution moves towards the next state in the sequence. It is easy to see that the periodic orbit gets attracted towards each of the states where either one or two of the components is ON (or 1) with the other components being OFF (or -1). The result is a periodic orbit traversing the six separate states of the device, giving a 3-fold symmetry. Later, we will see that the regions where the trajectory slows down are the locations of saddle node bifurcations.

Figure 3(b) shows that in this region of the parameter, λ, there is a very slow change in the period of oscillation, so the device is not very sensitive to perturbations. We observe that Fig. 2 is very representative of a wide range of λ values in this region of parameter space.

3.2. *Region II*: $\lambda \in (-0.6667, -0.5018)$

At $\lambda = -\frac{2}{3}$, there is a pitchfork bifurcation. Figure 1 shows that subsequently there are two new unstable equilibria. In addition, the origin loses its 1D stable manifold and has only eigenvalues with positive real part. The two new equilibria appear along the line $x_1 = x_2 = x_3$ and take over this line as their 1D stable manifolds. Figure 4(a) is representative for the dynamical behavior in this region of parameter space. As in the previous section, we find that all solutions of System (4), except those with initial conditions along the line $x_1 = x_2 = x_3$, converge to the stable limit cycle, which has changed very little

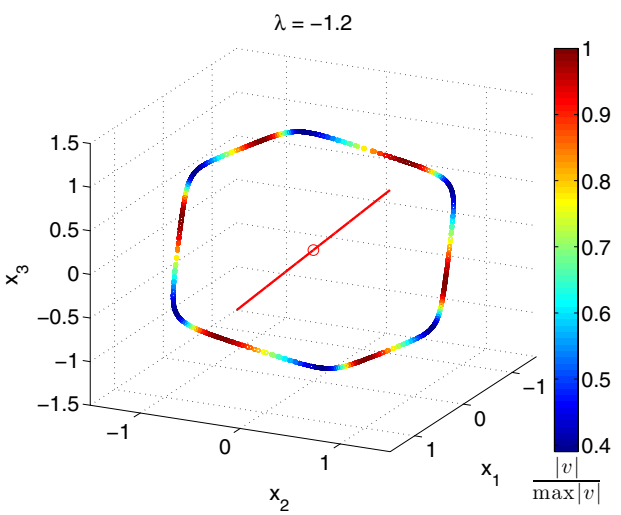

(a)

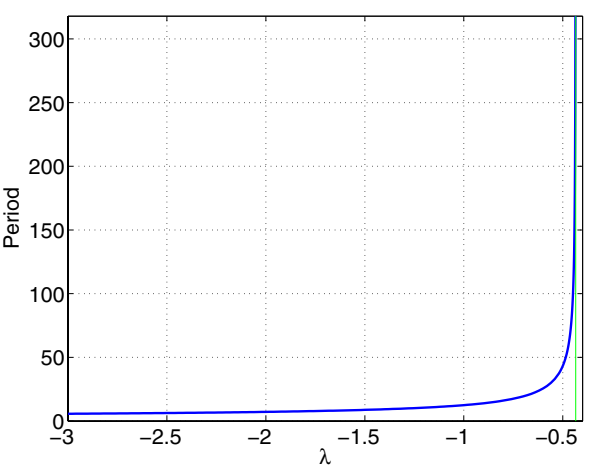

(b)

Fig. 3. For $\lambda = -1.2$, the stable limit cycle attracts all solutions of System (4), not along the line $x_1 = x_2 = x_3$. (a) Shows the velocity of the trajectory illustrating the slowing at the corners where the solution changes direction and (b) shows the length of the period of the orbit as λ varies.

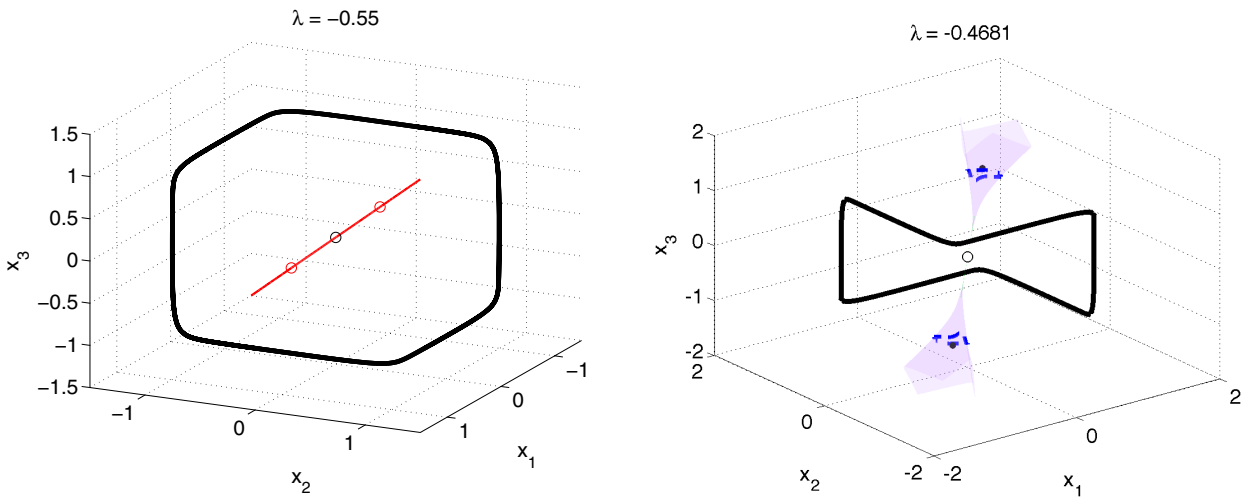

(a) (b)

Fig. 4. For (a) $\lambda = -0.55$ and (b) $\lambda = -0.4681$, the open black circle represents the unstable equilibrium at the origin. The black closed curve shows the stable limit cycle, which attracts all solutions of System (4), not along the line $x_1 = x_2 = x_3$ for (a) and outside the lavender pyramidal shaped regions for (b). In (a), the open red circles represent the symmetric unstable equilibria, which have 1D stable manifolds along the line $x_1 = x_2 = x_3$. For (b), the blue dashed line shows the unstable Hopf periodic orbit, which splits the lavender 3-sided pyramidal shaped region. The black solid circles along the line $x_1 = x_2 = x_3$ are the stable equilibria attracting all solutions inside the lavender pyramidal shaped regions.

from Fig. 2. Along the line $x_1 = x_2 = x_3$, the symmetric solution with $x_i > 0$ converges to the positive symmetric equilibrium, while if $x_i < 0$, then the solution of System (4) converges to the negative symmetric equilibrium. These symmetric equilibria are represented by open red circles in Fig. 4(a), while the origin becomes an unstable node, which is shown with an open black circle. The red lines represent the 1D stable manifolds emanating from the symmetric equilibria and are easily found by integrating backwards in time from the unstable, nontrivial equilibria. Again the period of the stable limit cycle is increasing, but not very rapidly, as seen in Fig. 3(b). Thus, the dynamics of System (4) change very little from the previous region for most initial conditions. However, there is fairly rapid divergence of the new unstable equilibria along the line $x_1 = x_2 = x_3$. The magnitude, $|\overline{x}_1|$, of the new symmetric equilibria increases from 0 to 0.8565, as λ varies from $-\frac{2}{3}$ to -0.5018. Thus, Fig. 4(a) shows the expected behavior for $\lambda \in (-0.6667, -0.5018)$ with the only major changes from varying λ being the distance between the symmetric equilibria.

3.3. *Region III*: $\lambda \in (-0.5018, -0.4475)$

The first major changes to the visualization of the dynamics of System (4) occur for λ in this range of values. The event that precipitates the change is a Hopf bifurcation, which allows the appearance of new symmetric basins of attraction. At $\lambda = -0.5018$, there is a subcritical Hopf bifurcation. This results in the significant change from the symmetric equilibria being unstable to becoming stable. Thus, there arises a local basin of attraction surrounding this equilibrium. Figure 4(b) provides a representative diagram for the basins of attraction for this range of λ values.

Immediately following the Hopf bifurcation at $\lambda = -0.5018$, unstable periodic orbits appear about the stable symmetric equilibria. Very slender conic regions passing through these periodic orbits appear around the line $x_1 = x_2 = x_3$ with the apex of these cones occurring at the origin. These conic regions become the basins of attraction for the new stable symmetric equilibria. The surface of the cones separate the initial conditions, which are attracted to the symmetric equilibria from the rest of 3-space where all other initial conditions lead to the large amplitude stable asymmetric periodic orbit. Thus, these cones become separatrices between the basins of attraction for the two stable equilibria and the periodic orbit.

The unstable Hopf periodic orbit is found using AUTO with XPPAUT [Ermentrout, 2002]. From the points generated by AUTO, we take points "near" this orbit, then integrate backwards in time

to create the 2D stable manifold separating the basins of attraction. The points closer to the origin from the Hopf periodic orbit produce the surface directed toward the origin, while the points further away create the surface of the cone in the direction away from the origin symmetrically about the line $x_1 = x_2 = x_3$. Near the Hopf bifurcation point $\lambda = -0.5018$, a very thin pencil shaped region follows the line $x_1 = x_2 = x_3$ and the Hopf periodic orbit is fairly circular with a period, $T \approx 18$. As λ increases, the unstable Hopf periodic orbit increases in amplitude, and its period increases. In addition, the orbit becomes more triangular in shape and less planar. Both of these features are observable in Fig. 4(b). Near $\lambda = -0.4475$, a homoclinic bifurcation occurs with the period of the unstable Hopf orbit going to infinity and the orbit tending to a triangular shape.

In summary, for the region where $\lambda \in (-0.5018, -0.4475)$, a subcritical Hopf bifurcation transforms two unstable equilibria along the line $x_1 = x_2 = x_3$ into symmetric stable equilibria. The periodic orbit produced by the Hopf bifurcation cycles around two conic shaped surfaces, which emanate from the unstable origin. These conic surfaces separate the two basins of attraction for the symmetric stable equilibria from the significantly larger region, which is a basin of attraction for the stable asymmetric periodic orbit. With increasing λ, the conic surfaces, which are centered about the line $x_1 = x_2 = x_3$, become larger in volume and take on a more triangular pyramidal shape, as seen in Fig. 4(b). They reach their maximum size around $\lambda = -0.4475$ with a homoclinic bifurcation. Another important feature, which we observe in Fig. 3(b) is that the length of the period of the stable asymmetric periodic orbit is increasing quite rapidly in this interval.

3.4. *Region IV*: $\lambda \in (-0.4475, -0.4346)$

At $\lambda = -0.4475$, there is a saddle node bifurcation with the appearance of 12 new equilibria. The onset of these equilibria occur near the corners of the triangular orbits from the unstable Hopf bifurcation just discussed. The new equilibria occur in pairs near the edges of the two symmetric pyramidal shaped basins of attraction for the two stable symmetric equilibria. These pairs have one unstable equilibrium, which has a 1D stable manifold (red) that runs along the edge of the pyramidal shaped

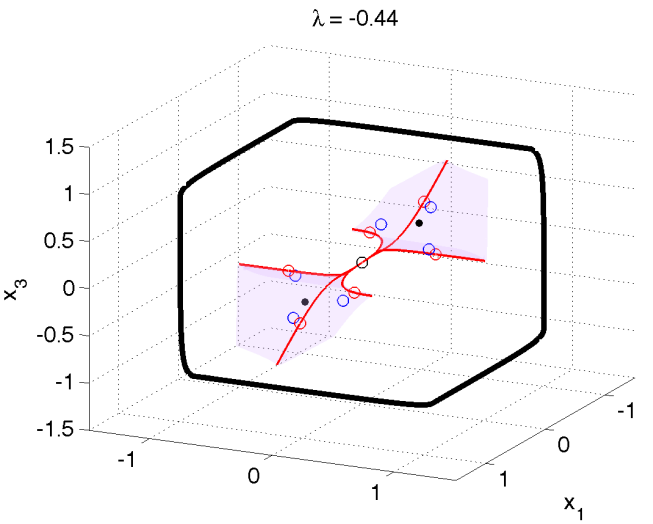

Fig. 5. Basins of attraction for $\lambda = -0.4400$. The open black circle represents the unstable equilibrium at the origin. The black closed curve shows the stable limit cycle, which attracts all solutions of System (4), outside the lavender pyramidal shaped regions. The red lines are the 1D stable manifolds for the unstable equilibria shown with the open red circles, and they form the edges of the lavender 3-sided pyramidal shaped regions. The open blue circles are the remaining six unstable equilibria with 2D stable manifolds, which form the faces of the lavender 3-sided pyramidal shaped regions. The black solid circles along the line $x_1 = x_2 = x_3$ are the stable equilibria attracting all solutions inside the lavender pyramidal shaped regions.

region, while the other unstable equilibrium has a 2D stable manifold (lavender), which creates the face of the pyramidal shaped region. Figure 5 is representative for this very small range of λ. The asymmetric stable periodic orbit continues to have the large basin of attraction, and its shape changes very little.

We observe that the pyramidal region continues to expand, making the basins of attraction larger for the two symmetric stable equilibria. Though the asymmetric periodic orbit looks similar to before, there is a significant change in its period. It approaches a homoclinic bifurcation at $\lambda = -0.4346$ with the period going to infinity. The trajectory spends significant time near the six corners listed in (5).

3.5. *Region V*: $\lambda \in (-0.4346, 0.4346)$

The interval of $\lambda \in (-0.4346, 0.4346)$ sees a wide range of change in the shapes of the basins of attraction. At $\lambda = -0.4346$, there is a saddle node bifurcation with 12 new equilibria appearing. These equilibria appear near the six corners of the asymmetric

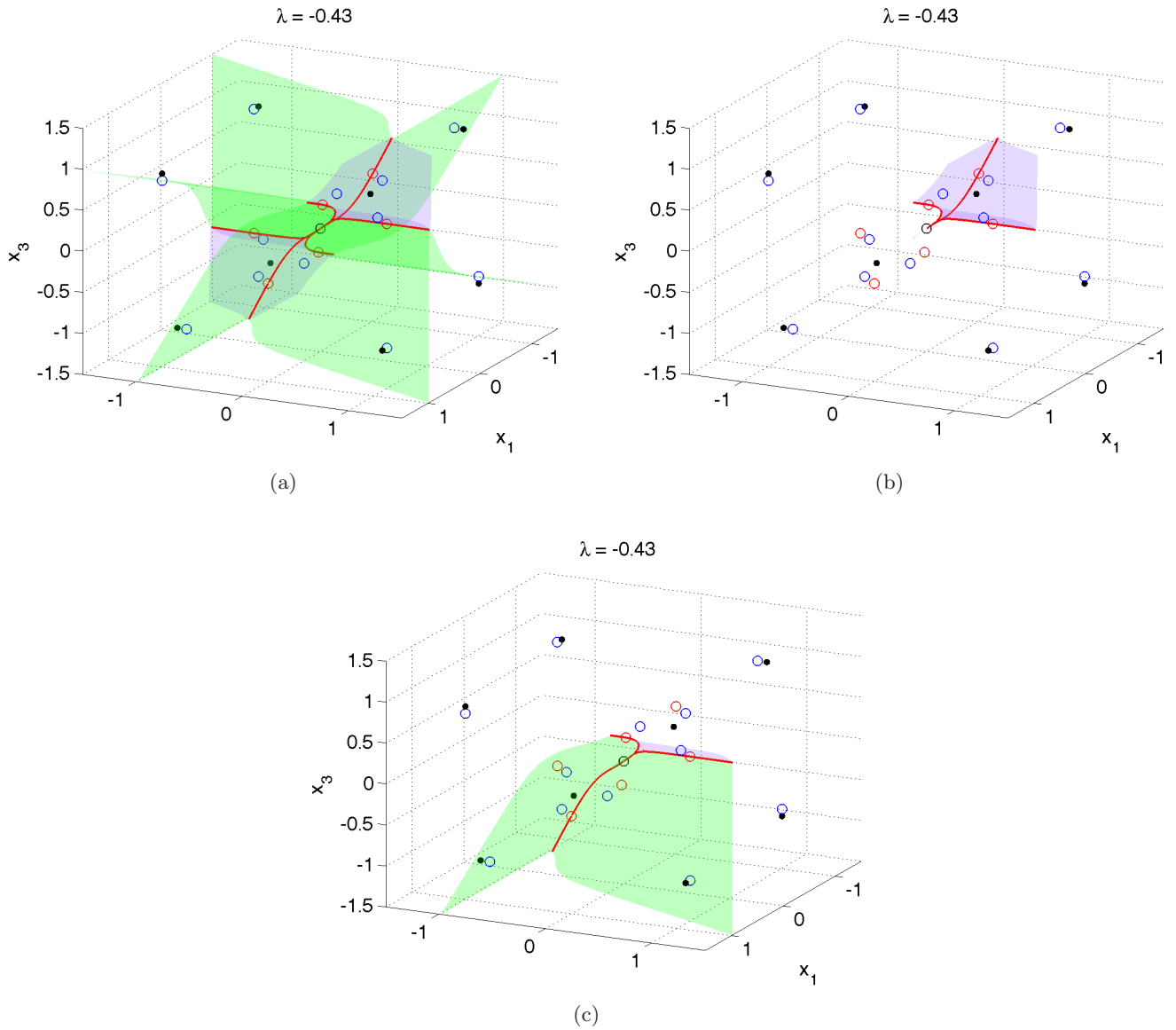

Fig. 6. (a) Basins of attraction for $\lambda = -0.4300$. The open black circle represents the unstable equilibrium at the origin. The red lines are the 1D stable manifolds for the unstable equilibria shown with the open red circles, and they form the edges of the lavender 3-sided pyramidal shaped regions. The open blue circles on the lavender surfaces are the remaining six unstable equilibria with 2D stable manifolds. They form the faces of the lavender 3-sided pyramidal shaped regions, which attract all solutions inside the black solid circles along the line $x_1 = x_2 = x_3$. There are six open blue circles on the green surfaces, with each connected to the red 1D stable manifolds. These green 2D stable manifolds separate the basins of attraction for the remaining six black solid circles, which are the asymmetric stable equilibria arising from the earlier heteroclinic stable orbit, (b) and (c) show one of the symmetric basins of attraction on top and one of the asymmetric basins of attraction on the bottom in isolation, respectively.

periodic orbit, which is lost. It follows that there are now 27 equilibria with eight of them being stable, which implies there are eight basins of attraction. Figure 6 shows how this region appears near the lower end of this region, shortly after the saddle node bifurcation. The pyramidal region (in lavender) is similar to the region seen in Fig. 5 where the 1D stable manifolds from six of the equilibria create the edges and the 2D stable manifolds from six other equilibria create the faces. The unstable node (black open circle) forms the apex of the two symmetric pyramidal basins of attraction for the two stable symmetric equilibria (black dots) along the line $x_1 = x_2 = x_3$ [see Fig. 6(b)]. The twelve new equilibria are divided into six stable nodes (black dots), which appear near the corners where

the former asymmetric period orbit slowed, and six more unstable equilibria (blue open circles) near the stable nodes, which have 2D stable manifolds. These 2D stable manifolds (green surfaces) intersect the 1D stable manifolds along the edges of the pyramidal basins of attraction, then project outward with a 3-fold symmetry. They create six basins of attraction for the six new stable nodes.

Figure 6(c) shows one of the six asymmetric basins of attraction. One face consists of one of the lavender faces, which has bound one of the two symmetric 3-sided pyramidal basins of attraction. As noted earlier, there are six pairs of new equilibria near the asymmetric points listed in (5). The pairs consist of a stable node and an unstable node with a 2D stable manifold. Figure 6(c) shows that each of the 2D stable manifolds (separatrices) have edges that connect one of the 1D stable manifold edges of one of the 3-sided pyramidal regions with the continuous extension through the origin of another 1D stable manifold edge of the other 3-sided symmetric pyramidal basin of attraction. This edge connects smoothly through the open blue circle (unstable equilibrium) to create another side of the separatrix. Similarly, another separatrix is formed by the next equilibrium pair near the progression given by (5). Only one of the stable equilibria is inside this region, and all solutions of System (4) inside this basin of attraction approach this particular equilibrium.

As λ progresses, the pyramidal shaped regions centered along the line $x_1 = x_2 = x_3$ continue expanding, while the other six basins of attraction contract. The asymmetric equilibria stay near the values listed in (5), while the unstable equilibria move closer to the faces of the octants in 3-space. When $\lambda = 0$, the coupling in System (4) is lost, and the shape of the basins of attraction can be seen in Fig. 7. The stable equilibria are all close to the eight points with x_1, x_2, and x_3 equal to either 1 or -1. The basins of attraction are bounded by the faces dividing each of the octants in 3-space with each face containing one of the 12 unstable equilibria with 2D stable manifolds. There are six unstable equilibria on each of the axes near ± 1 with 1D stable manifolds forming the edges of the basins of attraction, and the unstable node at the origin. Thus, each octant forms a basin of attraction for the eight stable nodes near the points listed in (5) and the two symmetric equilibria. Once again the lavender surfaces bound the symmetric stable equilibria,

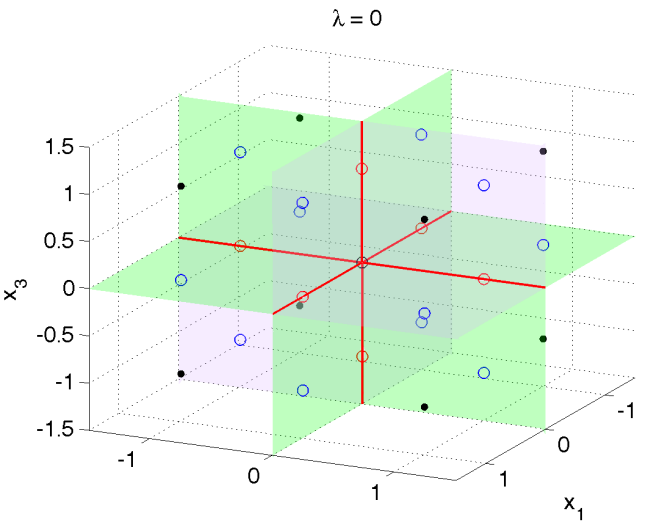

Fig. 7. Basins of attraction for $\lambda = 0$, the uncoupled system. The open black circle represents the unstable equilibrium at the origin. The basins of attraction are simply each of the octants. The positive and negative octants are separated by lavender planes and correspond to the symmetric equilibria. The remaining six octants hold the asymmetric stable equilibria separated by green planes along the axes. The 1D stable manifolds lie along the major axes.

while each of the other six stable equilibria have two green and one lavender 2D stable manifolds on the faces between each of the octants. We note that the six green 2D stable manifolds create a connected hyperplane with 3-fold symmetry that separates the symmetric stable equilibria. Understanding how this combined green hyperplane morphs is important in comprehending how the original 3-fold symmetric stable periodic orbit transitions to the 2-fold symmetric stable equilibria as λ increases.

As λ continues to increase toward a saddle node bifurcation at $\lambda = 0.4346$, the basins of attraction for the symmetric equilibria continue to expand as is visible in Fig. 8(b), where $\lambda = 0.4345$. The six asymmetric equilibria show basins of attraction spiraling out, which share one face from the basin of attraction for a symmetric equilibrium (lavender), and two other faces (green), which connect to the 1D stable manifolds passing through the open red circles and spiral into the unstable origin. This asymmetric basin of attraction is shown in Fig. 8(c). Significantly, in Fig. 8, the six asymmetric equilibria, which are near the points in (5), are coalescing with the six unstable equilibria (open blue circles) that are forming the lavender stable manifold and providing the separatrices between the symmetric and asymmetric equilibria. Also, we note that the

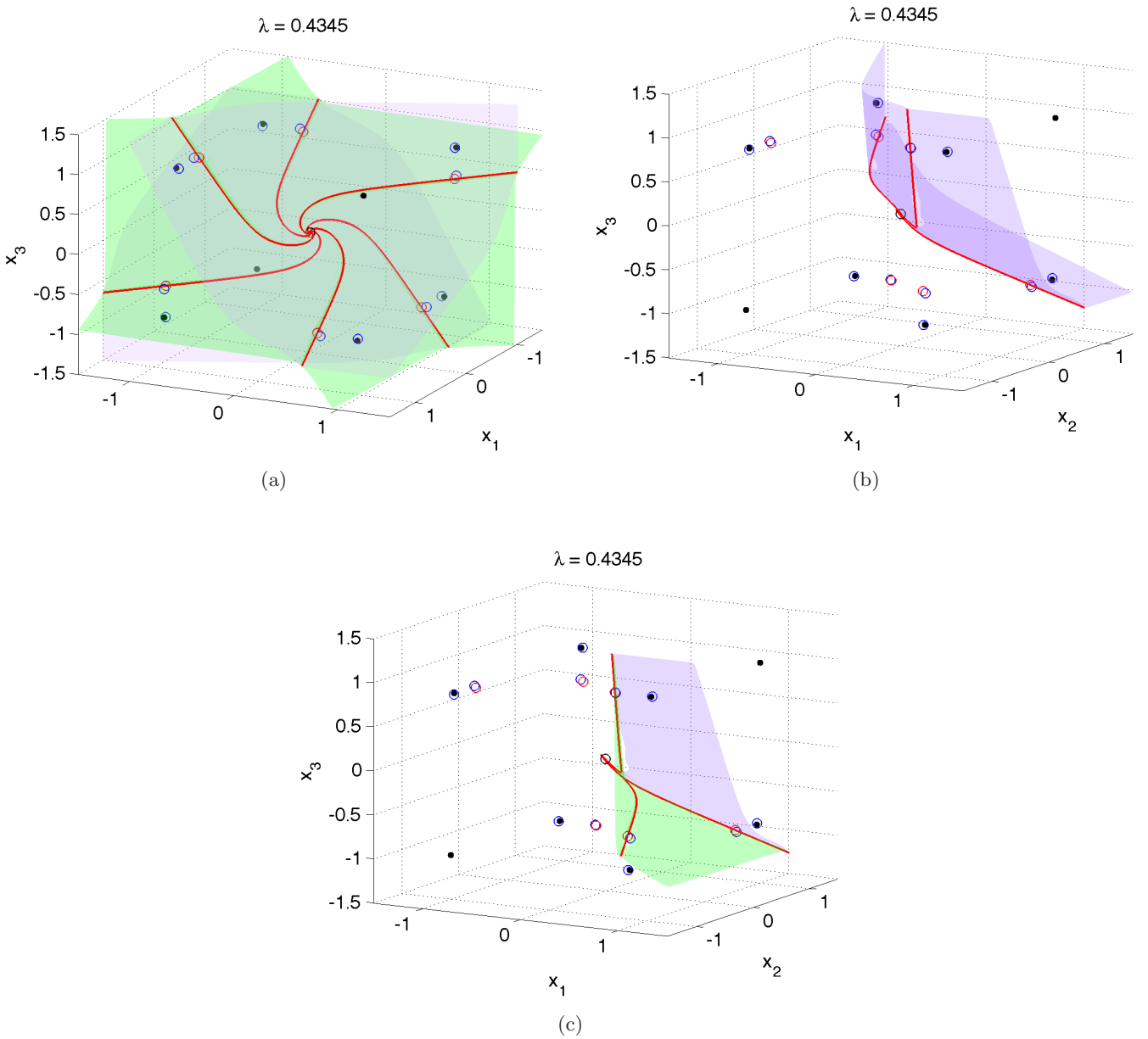

Fig. 8. (a) Basins of attraction for $\lambda = 0.4345$. The open black circle represents the unstable equilibrium at the origin. The red lines are the 1D stable manifolds for the unstable equilibria shown with the open red circles, and they form the edges of the lavender 3-sided pyramidal shaped regions. The open blue circles on the lavender surfaces are the remaining six unstable equilibria with 2D stable manifolds. They form the faces of the lavender 3-sided pyramidal shaped regions, which attract all solutions inside the black solid circles along the line $x_1 = x_2 = x_3$. There are six open blue circles on the green surfaces, with each connected to the red 1D stable manifolds. These green 2D stable manifolds separate the basins of attraction for the remaining six black solid circles, which are the asymmetric stable equilibria arising from the earlier heteroclinic stable orbit; (b) and (c) show one of the symmetric basins of attraction on top and one of the asymmetric basins of attraction on the bottom in isolation, respectively.

1D stable manifolds are spiraling closer to the points in (5), and the unstable equilibria (blue open circles) generating the asymmetric 2D stable manifolds (green) are approaching the unstable equilibria (red open circles) on the 1D stable manifold. It follows that all 24 asymmetric equilibria are relatively close to the six points in (5) in sets of four.

3.6. *Region VI*: $\lambda \in (0.4346, 0.4349)$

At $\lambda = 0.4346$, there is a saddle node bifurcation, and the six asymmetric stable equilibria and six unstable equilibria with 2D stable manifolds (lavender) disappear. This leaves the two stable symmetric equilibria attracting all solutions of System (4). The separatrix dividing these equilibria is composed of six asymmetric sections (green) from the 12 remaining unstable equilibria and the unstable origin. Figure 9(a) illustrates the positions of the various equilibria, the 1D stable manifolds (red), and the 2D stable manifolds (green). We note that this interval for λ is particularly small. Significantly, we observe that the 12 remaining equilibria have the open red circles and open blue circles, which generate the 1D and 2D stable manifolds, pairing very closely together. It is also significant that the 1D stable manifolds show a distinct spiraling shape, and the asymmetric equilibria are located near the points in (5). As seen in Fig. 1, the next saddle node bifurcation occurs near the end of this interval with $\lambda = 0.4349$, so follows very rapidly in parameter space.

3.7. *Region VII*: $\lambda \in (0.4349, 1.3333)$

For $\lambda \in (0.4349, 1.3333)$, there is a 2D stable manifold, which contains an unstable Hopf periodic orbit. This manifold is a separatrix for the basins of attraction for the two stable symmetric equilibria. Except for initial conditions on the stable manifold, all solutions of System (4) approach one of the stable symmetric equilibria with $x_{1e} = x_{2e} = x_{3e} \approx \pm 1$.

Beginning at $\lambda = 0.4349$, we have a saddle node bifurcation, losing the twelve unstable equilibria seen in Fig. 9(a). This is also where from the right, there is a homoclinic bifurcation. This value of λ sees the period of the unstable Hopf periodic orbit go to infinity. Approaching from the right, the trajectory around the limit cycle spends increasing time near the locations, where the new equilibria ultimately appear from the saddle node bifurcation.

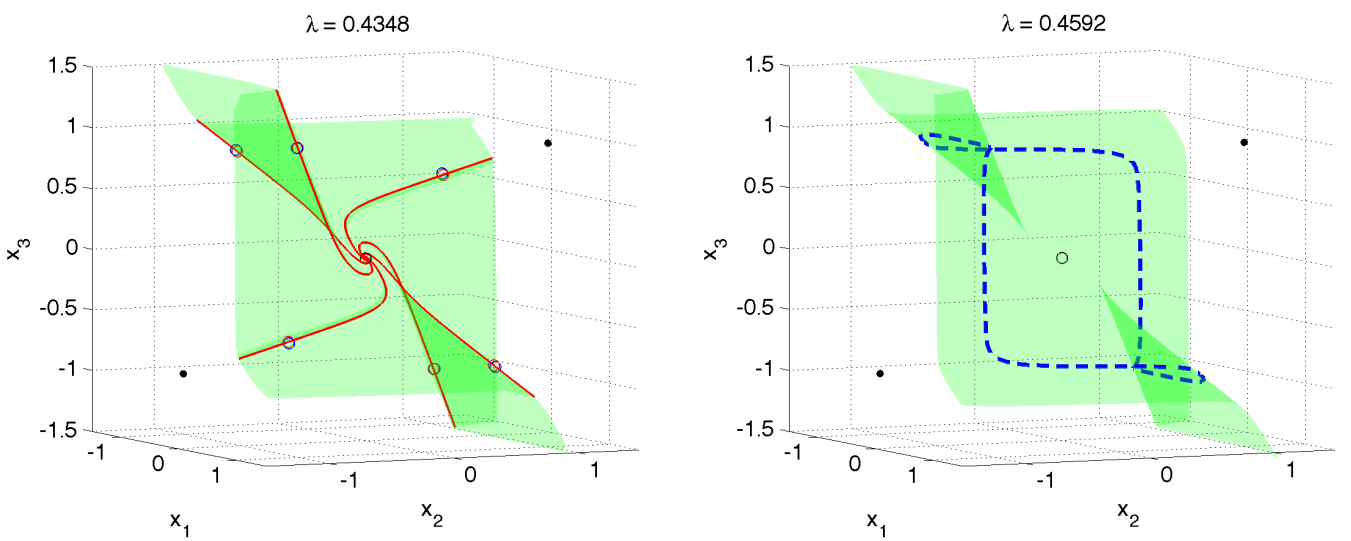

(a) (b)

Fig. 9. For (a) $\lambda = 0.4348$ and (b) $\lambda = 0.4592$, the open black circle represents the unstable equilibrium at the origin. For (a) $\lambda = 0.4348$, the 12 other unstable equilibria shown with open red and blue circles are closely aligned, and their 1D and 2D stable manifolds create this 3-fold symmetric hyperplane in six pieces, which separate the two stable symmetric equilibria (solid black circles). The spiral shape and closeness of the unstable equilibria are indicative of the smooth transition through the next saddle node bifurcation seen in (b) where, for $\lambda = 0.4592$, there is a blue dashed line for the periodic orbit from the unstable Hopf bifurcation at $\lambda = 1.3333$. The green hyperplane is the 2D stable manifold, which arises from this periodic orbit and splits the space into only two basins of attraction. The trajectories, except those on the 2D stable manifold (separatrix), asymptotically approach the two symmetric stable equilibria shown as solid black circles.

Examining Fig. 9, we see that the locations of the unstable equilibria in Fig. 9(a) are very close to the corners of the limit cycle in Fig. 9(b). These corners of the limit cycle approach the positions in (5), so this unstable Hopf periodic orbit has a similar shape to the stable limit cycle when $\lambda < -0.5018$. However, the direction of the trajectory is reversed. It is worth noting that the 3-fold symmetric shape of the separatrix is very similar for both graphs in Fig. 9, demonstrating the continuity in λ.

As λ increases in this interval, the amplitude of the unstable periodic orbit decreases and becomes more circular. In addition, the 2D stable manifold becomes flatter. These changes continue until the point of the subcritical Hopf bifurcation at $\lambda = \frac{4}{3}$. Numerically, the 2D stable manifold is generated by taking points near the periodic orbit and integrating System (4) backwards in time. Initial conditions closer to the origin tend to the origin, while initial conditions further away form the remainder of this 2D separatrix.

3.8. *Region VIII*: $\lambda > 1.3333$

After $\lambda = \frac{4}{3}$, the origin gains two eigenvalues with negative real part. This results in a 2D stable manifold emanating from the origin. Numerically, this 2D manifold is found by taking initial conditions near the origin and integrating backwards in time. Figure 10(a) is representative of this region with the two symmetric stable equilibria having $x_{1e} = x_{2e} = x_{3e} \approx 1$, appearing as solid black dots. It shows

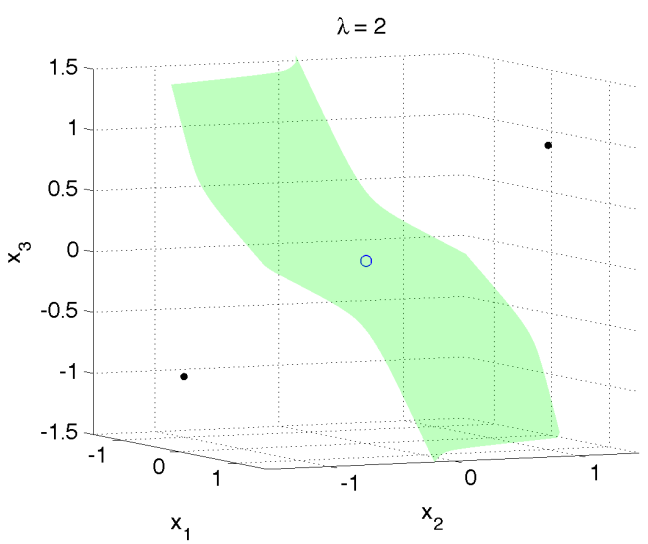

Fig. 10. For $\lambda = 2$. The trajectories, except those on the 2D stable manifold (separatrix), asymptotically approach the two symmetric stable equilibria shown as solid black circles.

the origin with a blue open circle surrounded by a green 2D stable manifold separating the basins of attraction for the two symmetric stable equilibria.

3.9. *System flow and continuity*

It is important to note that the vector field flow of a system of ordinary differential equations (ODEs), like System (4), is continuous. Bifurcations result in changes of behavior, but these changes occur in a smooth continuous manner. The previous sections have shown the changes in the basins of attraction, which vary over a wide range. In this section we show more details on the nature of the transitions based on the solution trajectories of System (4).

When the coupling parameter, λ, is sufficiently negative, System (4) has the globally attracting periodic orbit with its circulation being positive relative to the 1D stable manifold of the origin with directional vector $\langle 1, 1, 1\rangle$. (See Fig. 2.) This 1D stable manifold with its symmetric equilibria develops thin symmetrical conical basins of attraction, which expand continuously as λ increases. These symmetric basins of attraction have the vector field flow near the unstable Hopf periodic orbit matching the stable limit cycle. [See Fig. 4(b).] The loss of the unstable Hopf cycle through a homoclinic bifurcation and saddle node bifurcation results in little geometric change of the symmetric basins of attraction, which have morphed into triangular pyramidal shaped cones. For λ in this range, most trajectories have some component with the positive circulation noted above. These trajectories tend to either the stable symmetric equilibria or the stable limit cycle. However, there is also directional flow along the 1D stable manifolds in the direction of the unstable equilibria arising from the saddle node bifurcation. Figure 11(a) shows the existence of a strong directional component of the solution trajectories toward the corners of the stable limit cycle, where the solution spends the most time. [See Fig. 3(a).] At $\lambda = -0.4346$, the heteroclinic stable limit cycle has its period go to infinity [Fig. 3(b)], and the saddle node bifurcation results in six stable nodes attracting the trajectories of System (4). Figure 11 shows this transition. While at first glance the graphs appear very different, close inspection shows the trajectories traveling very similar paths. Though there is a periodic orbit in Fig. 11(a), the solution trajectories spend very long times near the corners, where the six stable equilibria appear after the saddle node bifurcation.

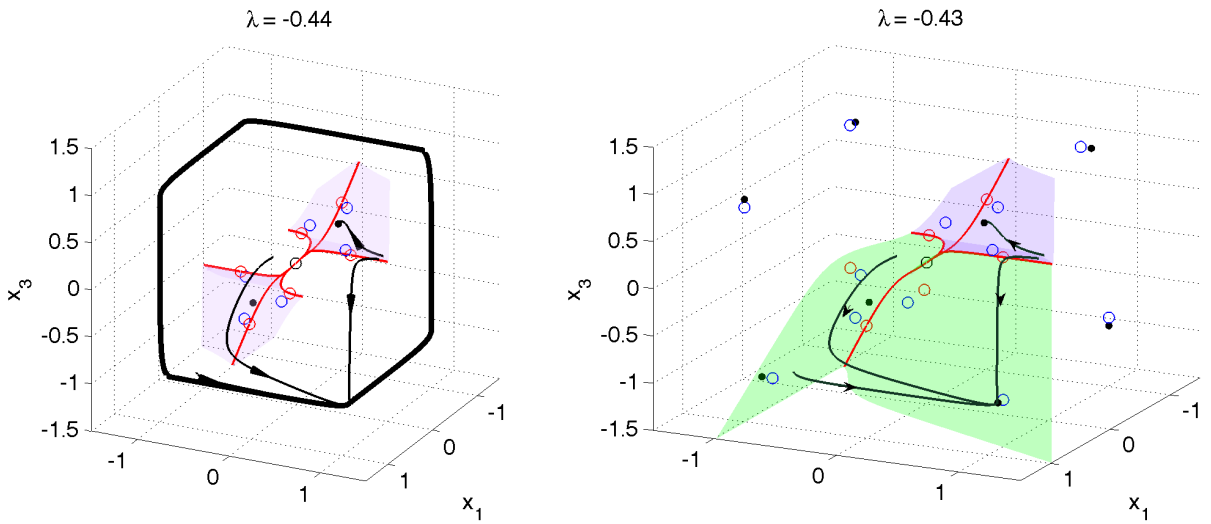

(a) (b)

Fig. 11. For (a) $\lambda = -0.44$ and (b) $\lambda = -0.43$, the equilibria, periodic orbits, and some 1D and 2D stable manifolds are shown. Four solution trajectories for System (4) are shown. These trajectories follow very similar paths, showing continuity of the flow.

Figure 12 provides another example, where at first glance the transition from eight basins of attraction on the left to only two basins of attraction on the right appears discontinuous. However, careful examination of the five trajectories plotted in the two graphs show they closely track each other. Three of the trajectories in Fig. 12(a) approach the stable asymmetric equilibrium, while the two starting in the basin of attraction for the symmetric equilibrium asymptotically approach it after first tracking toward the stable asymmetric equilibrium. In Fig. 12(b), we see the three solution trajectories trending toward the point where the asymmetric equilibrium had been, then turning and tracking toward the symmetric equilibrium. These trajectories slow considerably as they near the location where the asymmetric equilibrium had been. Thus, we see a continual evolution of vector field flow, despite changes in the numbers of basins of attraction and equilibria.

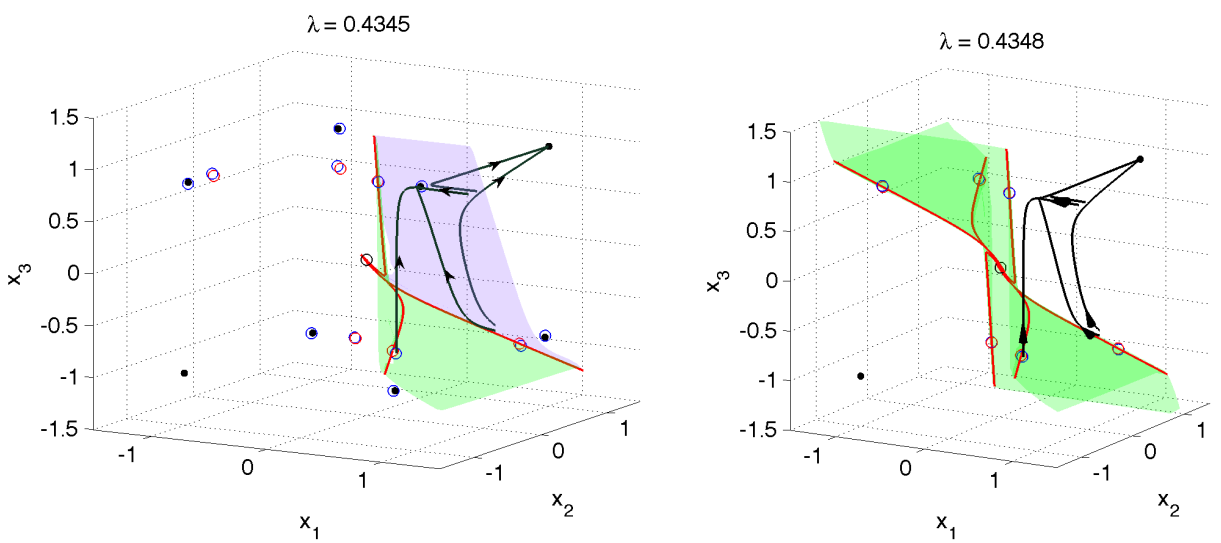

(a) (b)

Fig. 12. For (a) $\lambda = 0.4345$ and (b) $\lambda = 0.4348$, the equilibria and some 1D and 2D stable manifolds are shown. Five solution trajectories for System (4) are shown. These trajectories follow very similar paths, showing continuity of the flow.

4. Methods

In dynamical systems theory, it is well known that stable (or unstable) manifolds form the boundaries between the basins of attraction for the dynamical attractors of a system. Computing stable manifolds is, however, not a trivial task. In general, closed form expressions for these manifolds cannot be obtained. Thus, we must resort to specialized numerical methods to compute the stable and unstable manifolds. Many approaches have been formulated [Krauskopf & Osinga, 1999; Henderson, 2003; Dellnitz & Hohmann, 1997; Doedel *et al.*, 1991a, 1991b; Guckenheimer & Vladimirsky, 2004]. A good review article summarizing a variety of methods is [Krauskopf *et al.*, 2005]. Each of these methods was used to compute the "Lorenz Manifold," the two-dimensional stable manifold of the origin in the Lorenz system, which is, in effect, a three-dimensional problem. In the case of the present paper, the problem is effectively four-dimensional since the stable manifolds of the coupled bistable system [Eq. (2)] are studied computationally as the coupling parameter λ evolves. Since stable manifolds of saddle points and unstable limit cycles are computed, a few simple but carefully developed techniques are needed to compute the stable manifolds as λ is varied.

The techniques used to produce the figures in this paper are described in this section. There are as many as 27 equilibria, which have to be found numerically. The saddle node equilibria have either 1D or 2D stable manifolds, which need to be found and graphed. Finally, there are two Hopf bifurcations with unstable periodic orbits, which have to be tracked and used to find 2D stable manifolds. Details of the numerical implementation are presented from a dynamical systems perspective, so that the computations may be performed for many other systems. The majority of the computational work and graphics are done in MatLab, and the code used to generate the figures in this paper is available at the online repository [Lyons *et al.*, 2014].

4.1. *Equilibrium continuation*

The qualitative study of any system of ODEs begins with finding and analyzing all equilibria for the system. For System (4), the derivatives are set equal to zero, and the nonlinear system of equations is solved to find equilibria. It is apparent that the origin $(0, 0, 0)$ is one equilibrium for this system independent of λ. However, all other equilibria are found using numerical methods. In addition to finding equilibria, we need the eigenvalues and eigenvectors from the linearization about the equilibria, which uses the Jacobian of the RHS of System (4):

$$J(x_1, x_2, x_3; \lambda) = \begin{pmatrix} -1 + c\,\mathrm{sech}^2(c(x_1 + \lambda x_2)) & c\lambda\,\mathrm{sech}^2(c(x_1 + \lambda x_2)) & 0 \\ 0 & -1 + c\,\mathrm{sech}^2(c(x_2 + \lambda x_3)) & c\lambda\,\mathrm{sech}^2(c(x_2 + \lambda x_3)) \\ c\lambda\,\mathrm{sech}^2(c(x_3 + \lambda x_1)) & 0 & -1 + c\,\mathrm{sech}^2(c(x_3 + \lambda x_1)) \end{pmatrix}.$$

There are a number of methods for finding the many equilibria for System (4). Perhaps the most efficient way to find equilibria is using AUTO in the software package XPPAUT [Ermentrout, 2002]. From the known equilibrium at the origin, AUTO can track equilibria and periodic orbits, as it finds bifurcations by varying λ, which give rise to new equilibria. For System (4), the easiest way to find and track equilibria is to start with the case $\lambda = 0$, the uncoupled system. This particular case sees each equation having its dynamics independent of the other. It follows that the equilibria are found by solving:

$$-x_i + \tanh(cx_i) = 0,$$

which for $c = 3$ gives $x_{ie} = 0$ being unstable and $x_{ie} = \pm 0.9949$ being stable in the x_i direction. For System (4) at $\lambda = 0$, there are 27 equilibria from all the possible combinations of the three equilibria for each of the three components. Furthermore, the information on the stability of each component transfers to the entire system. It follows that there are eight stable nodes from all combinations of

$$(x_{1e}, x_{2e}, x_{3e}) = (\pm 0.9949, \pm 0.9949, \pm 0.9949).$$

The origin is clearly an unstable node. The equilibria with one component, $x_{ie} = 0$, and the other two components having $x_{je} = \pm 0.9949$, $j \neq i$, produce

12 unstable saddle nodes with 2D stable manifolds. These 2D stable manifolds align with the coordinate planes in each of the octants. Finally, there are six unstable saddle nodes with two components satisfying $x_{ie} = 0$ and the remaining one having $x_{je} = \pm 0.9949$. These equilibria have 1D stable manifolds along the coordinate axes.

With these equilibria established for System (4) with $\lambda = 0$, the `fsolve` routine in MatLab is used in a program to find the equilibria for other λ. The `fsolve` routine uses a Levenberg–Marquardt method to solve the vector system:

$$\mathbf{F}(\mathbf{x}, \lambda) = \mathbf{0},$$

for $\mathbf{x}$. One of the equilibria above is used as initial conditions, then λ is varied slowly in the positive and negative directions over the desired domain or until a saddle node bifurcation is encountered. At each step of the procedure for computing new equilibria, the new value of λ is entered with the previously computed equilibrium value used as an initial guess. MatLab's `fsolve` routine can readily find a new equilibrium unless we are very close to a saddle node bifurcation. If we are close to a saddle node bifurcation, then the stepsize of λ is reduced to obtain the new equilibrium value. If the initial equilibrium, (x_{1e}, x_{2e}, x_{3e}), is an asynchronous equilibrium point, then symmetry automatically produces five more equilibria: (x_{2e}, x_{3e}, x_{1e}), (x_{3e}, x_{1e}, x_{2e}), $(-x_{1e}, -x_{2e}, -x_{3e})$, $(-x_{2e}, -x_{3e}, -x_{1e})$, and $(-x_{3e}, -x_{1e}, -x_{2e})$. Furthermore, all six of these equilibria maintain the properties, like unstable saddle node with a 2D stable manifold, which agree with the properties of the initial equilibrium at $\lambda = 0$. These properties are easily checked at any equilibrium by finding the eigenvalues of the Jacobian matrix, $J(x_{1e}, x_{2e}, x_{3e}; \lambda)$, at the equilibrium.

Even though there are 27 equilibria, there are only six qualitatively different ones. The eight stable equilibria divide into two categories with the two symmetric equilibria and the six asymmetric equilibria. There are 12 asymmetric equilibria with 2D stable manifolds, which also divide into two categories. The first six are the ones, which when $\lambda = 0$, border on the faces of Octant I or its negative, Octant VII, generating the lavender separatrices, and the other six come from the remaining equilibria on the faces of the other Octants when $\lambda = 0$, generating the green separatrices. Finally, the six equilibria on the coordinate axes when $\lambda = 0$

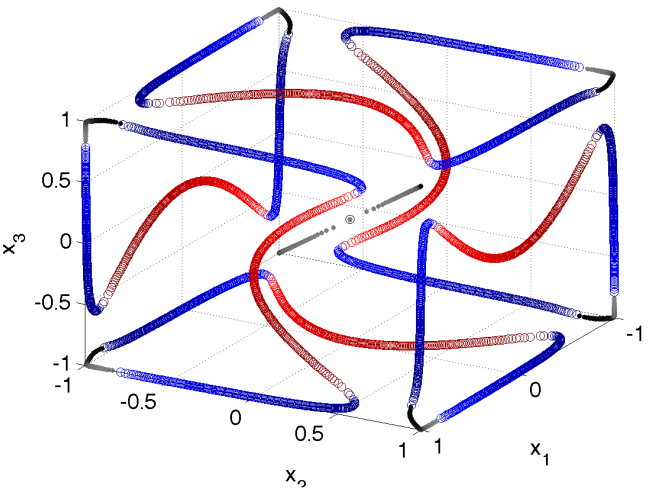

Fig. 13. There are 27 equilibria shown in this diagram at various values of λ. Three are the origin and the two symmetric equilibria. There are 24 asymmetric equilibria, which over the range of λ connect in a long chain. The gray-black equilibria are stable. The blue equilibria have 2D stable manifolds, and the red equilibria have 1D stable manifolds. The darker the shade of blue or red the higher the value of λ. Changes in color occur at saddle node bifurcations. All 27 equilibria can be arranged into one of four group orbits generated by the symmetry group $\Gamma \simeq \mathbf{Z}_2^3 \otimes \mathbf{Z}_3$. Then this plot can be interpreted as a color-coded evolution of four distinct group orbits as a function of λ. A gray-black straight line for the graph of the group orbit of two symmetric equilibria, including the origin and three additional curves, red, blue and gray, for the 24 asymmetric equilibria.

generate the equilibria with 1D stable manifolds. Figure 13 shows the evolution of these different types of equilibria as λ varies. The origin remains a fixed, unstable equilibrium with some of its eigenvalues changing sign only at the point of the pitchfork bifurcation ($\lambda = -0.6667$) and the subcritical Hopf ($\lambda = 1.3333$). Consider first the two symmetric equilibria and recall the 24-elements group $\Gamma \simeq \mathbf{Z}_2^3 \otimes \mathbf{Z}_3$ of symmetries of the coupled bistable system, see Sec. 2. Reflections send one of the symmetric equilibria (x, x, x) to the other $(-x, -x, -x)$, and vice versa, while cyclic rotations leave them unchanged. In other words, the pair of symmetric equilibria are in the group orbit generated from the symmetry group $\Gamma \simeq \mathbf{Z}_2^3 \otimes \mathbf{Z}_3$. Thus, from a symmetry standpoint, these two equilibria are one and the same. Upon changing λ, the group orbit evolves while it tracks the line $x_1 = x_2 = x_3$, starting at $\lambda = -0.6667$ and both equilibria on the orbit become stable (as expected because they are in the same group orbit) after the subcritical Hopf bifurcation at $\lambda = -0.5018$. The resulting equilibria are

visible as the straight-line segment shades from gray to black in the middle of Fig. 13.

Figure 13 shows that the asymmetric stable equilibria track six small curves remaining near the points given in (5). Similarly, these equilibria are symmetrically related and share stability properties, since they are in the same (second) group orbit generated by Γ. The small curves track from gray to black as $\lambda \in (-0.4346, 0.4346)$ varies. The gray end of the curve connects to one set of six equilibria with 2D stable manifolds, which are shown in Fig. 13, starting with the lighter blue and becoming darker as $\lambda \in (-0.4346, 0.4349)$ varies. This particular set generates the green 2D stable manifolds in our previous figures, and when $\lambda = 0$, these curves pass through a point (x_{1e}, x_{2e}, x_{3e}), where the x_{ie}, $i = 1, 2, 3$, is a permutation of the values -0.9949, 0, and 0.9949. The permutation is equivalent to applying the 24-elements of the symmetry group Γ, which yields a total of 12 asymmetric unstable nodes connected in a third group orbit. The dark end of these six blue curves match the dark end of the six red curves at the saddle node bifurcation when $\lambda = 0.4349$. The six red curves sweep a long arc passing through one of the coordinate axes near $x_{ie} = \pm 0.9949$ for some $i = 1, 2, 3$, where six additional unstable saddle nodes are located. These six saddle node points form the fourth group orbit of equilibria. As the red becomes lighter, these curves reach another saddle node bifurcation at $\lambda = -0.4475$, where they match with the light end of the other set of six blue curves. This set of six blue curves of equilibria have 2D stable manifolds, which are lavender in the previous figures, separating the symmetric equilibria from the asymmetric equilibria. When $\lambda = 0$, these equilibria are on one of the coordinate planes with two values of x_{ie} being either ± 0.9949 and the other being $x_{je} = 0$. These six curves become darker as λ increases to 0.4346, where the lavender stable manifolds vanish at a saddle node bifurcation. This saddle node bifurcation has the dark blue curve match the black of another asymmetric stable equilibrium at a different adjacent corner.

In summary, the 24 asymmetric equilibrium points can be arranged into one of three distinct group orbits. Thus, Fig. 13 can be interpreted as a color-coded evolution of four distinct group orbits as a function of λ, which yields: a straight-line in the middle connecting the two symmetric equilibria $(\pm x, \pm x, \pm x)$ and the origin; six gray-to-black corner segments connecting six asymmetric stable nodes of the form $(\pm x, \pm x, \mp x)$; 12 blue curves for the group orbit of 12 asymmetric unstable nodes with representative $(0, \pm x, \pm x)$; six red curves which connect the remaining six asymmetric unstable saddle nodes of the type $(0, 0, \pm x)$. All other equilibria can be readily obtained by applying directly the 24-elements of the group Γ to the representative elements listed above. We observe in Fig. 13 that if one begins at any one of the asymmetric equilibria and increases and decreases λ between the saddle node bifurcation values, then one can continuously reach all the remaining 23 asymmetric equilibria. This property deserves further investigation. The codes used to generate these equilibria are available at [Lyons *et al.*, 2014].

4.2. *Periodic orbits*

The stable limit cycles for $\lambda < -0.4346$ were obtained by forward numerical integration, starting with an initial condition near one of the points in (5) and retaining values for sufficiently large t. The unstable limit cycles, coming from the subcritical Hopf bifurcations with $-0.5018 < \lambda < -0.4475$ and $0.4349 < \lambda < 1.3333$, were computed with AUTO in XPPAUT.

4.3. *1D stable manifolds*

The 1D stable manifolds are important features in our diagrams showing the basins of attraction. They divide many of the 2D separatrices bounding the basins of attraction for the stable equilibria. The computation of the 1D stable manifolds is quite easy, given the equilibrium. The unstable saddle node, $\mathbf{x}_e$, has exactly one negative eigenvalue, and the Jacobian matrix, $J(\mathbf{x}_e; \lambda)$, is used to obtain the associated eigenvector, $\mathbf{v}_e$. Two initial conditions, $\mathbf{x}_0 = \mathbf{x}_e \pm \delta \mathbf{v}_e$, for small δ are taken, and then System (4) is numerically integrated with MatLab's `ODE23` in reverse time. The numerical integrations are carried out sufficiently far back in time to provide adequate points that map the entire 1D stable manifold for a particular figure.

4.4. *2D stable manifolds*

The 2D stable manifolds extend from an unstable node with two eigenvalues with negative real part. The two corresponding eigenvectors form a basis for the 2D linear eigenspace at the equilibrium point,

and this linear eigenspace is tangent to the 2D stable manifold at the saddle point. Our procedure for finding this 2D stable manifold follows an extension of the procedure noted above for finding 1D stable manifolds. In this case, a locus of many points lying in the 2D stable linear eigenspace of the saddle point are initial conditions for numerical integration in reverse time. A large number of solution values are to be saved from each trajectory. If all of the points are plotted simultaneously in Matlab using `plot3` with markers, a surface formed by the points should be visually apparent. Once these points have been obtained, a triangulation algorithm can be implemented to construct the 2D stable manifold. The well-known Delaunay triangulation algorithm, which is implemented in Matlab with the `delaunay` function, may be used to triangulate the surface. In this work, the open source function `Delaunay2_5D`, which implements the `delaunay` function, is used. The function `Delaunay2_5D` outputs a three column matrix, each row of which represents the corresponding array indices of x_1, x_2, and x_3 points each triangle. Once the triangle indices have been obtained, the Matlab function `trisurf` is used to plot the surface in 3D. More details about obtaining smooth edges of the surface and the implementation are available in Appendices A and B.

For the computation of 2D stable manifolds arising from unstable limit cycles from Hopf bifurcations, a full period of the unstable periodic orbit is obtained from AUTO in XPPAUT. Figure 1 shows that the unstable Hopf bifurcations arise from the branches of the three synchronous equilibria. AUTO uses a numerical boundary value approach, which also computes the period accurately [Doedel, 2010]. XPPAUT stores the numerical values for the unstable periodic orbit for each value of λ, and the user can "grab" each of these orbits and export the data into a text file.

After importing the unstable limit cycle orbit into MatLab, the corresponding 2D stable manifold may be obtained with backward (in time) numerical integration of a small set of initial conditions. For each 3D orbit point, a cube of initial conditions is generated around the point with small perturbations parallel to the coordinate axes, as described in Appendix A. Backward numerical integration is used to obtain a large number of points on the manifold that may be plotted with the MatLab `plot3` command so that the stable manifold is visually apparent. The remainder of the procedure for obtaining the stable manifolds is the same as for computing 2D stable manifolds of saddle points, as described above.

5. Discussion

A complete study of the basins of attraction for a ring of bistable equations coupled unidirectionally has been presented. The System (2) has a range of behaviors as the coupling strength varied. The ring exhibits spatial global symmetries defined by $\mathbf{Z}_N$, the group of cyclic permutations of N objects. Each unit, in turn, possesses internal reflectional symmetries. Together, these symmetries lead to complex patterns of collective behavior. For large, and negative values of coupling strength λ and $N = 3$, a branch of globally asymptotically stable limit cycle oscillations define the long-term dynamics. These limit cycle oscillations emerge at small values of λ through a heteroclinic cycle connecting multiple asymmetric equilibria. For large positive values of λ all trajectories converge to one of two symmetrical and stable equilibrium points. The transition from these stable equilibrium points to the limit cycles as a function of λ was discussed in great detail through 3D visualizations of the basins of attractions for all invariant sets that appear in between. In spite of the changes in the collective behavior the basins of attraction vary smoothly as λ changes.

Our study uses the Stable Manifold Theorem to numerically find the separatrices between the basins of attraction. The 1D and 2D stable manifolds, which create the edges and surfaces bounding the basins of attraction, are readily found by starting near appropriate equilibria and integrating backwards in time. When a sufficient number of trajectories are simulated, then a triangulation scheme in MatLab allows construction of the surface approximating the separatrix. The symmetries inherent in this system simplify finding the complete set of bounding surfaces for the basins of attraction. In lieu of a 3D animation, a montage of the distinct geometric structures defined by the basins of attraction is illustrated in Fig. 14. (See Appendix for links to movies showing the evolution of the basins of attraction as coupling strength varies.)

Our results show how a dynamical system can smoothly evolve from a 3-fold symmetric large amplitude stable periodic orbit attracting almost all solutions of System (4) to a 2-fold symmetric

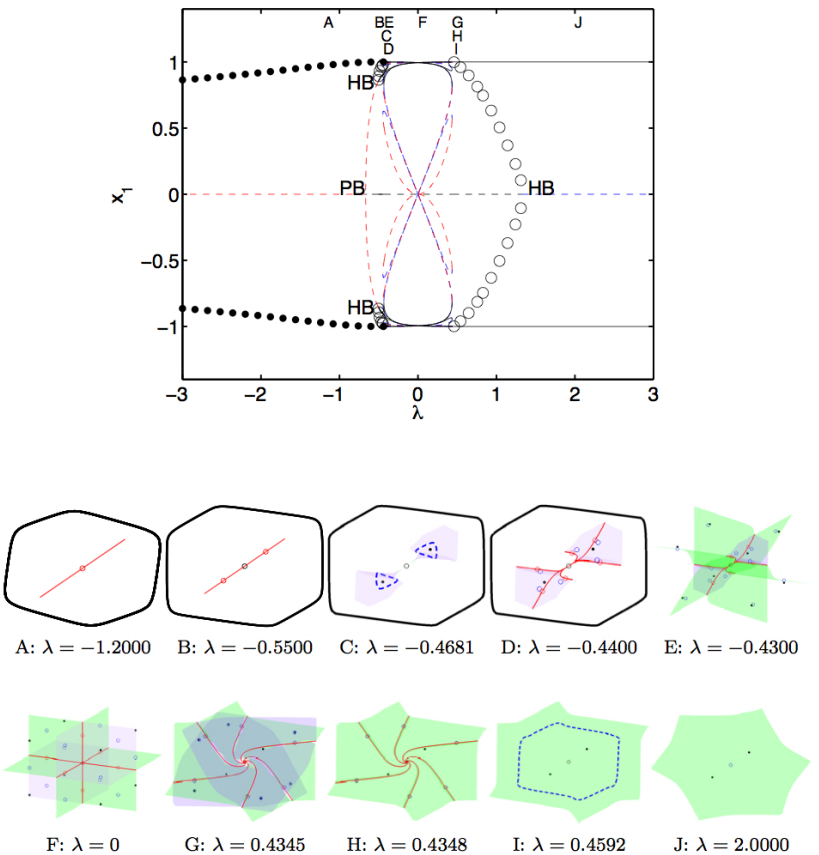

Fig. 14. Montage of the geometric structure of the basins of attraction of a ring of bistable units connected unidirectionally. A detailed description of each figure is provided throughout the manuscript.

situation, where almost all solutions are attracted to only two stable equilibria. The varying coupling strength of this 3D bistable system causes multiple bifurcations, including a pitchfork, two subcritical Hopf, and four saddle node bifurcations. We demonstrated how each of these bifurcations affected changes that create, destroy, or vary the shape of the basins of attraction, allowing smooth transitions to alter the observed dynamical behavior.

This work has been motivated by previous analysis of the basins of attraction of coupled bistable systems subject to delay [Lyons *et al.*, 2010]. Similar behaviors are observed for larger (odd) values of N with the additional appearance of unstable branches of limit cycles through Hopf bifurcations. For even values, neither heteroclinic connections nor stable oscillations exist. The specific visualization methods employed here are clearly limited to 3D systems of differential equations. However, our methods are sufficiently general to be applied to study other coupled bistable systems with different symmetry groups.

Acknowledgments

A. Palacios was supported by the Complex Dynamics and Systems Program of the Army Research Office, supervised by Dr. Samuel Stanton, under grant W911NF-07-R-003-4. He was also supported by the ONR Summer Faculty Research Program, at SPAWAR Systems Center, San Diego. V. In acknowledges support from the Office of Naval Research (Code 30) and the SPAWAR internal research funding (S&T) program.

References

Ajo-Franklin, C. M., Drubin, D. A., Eskin, J. A., Gee, E. P. S., Landgraf, D., Phillips, I. & Silver, P. A. [2007] "Rational design of memory in eukaryotic cells," *Genes Develop.* **21**, 2271–2276.

Bulsara, A., In, V., Kho, A., Longhini, P., Palacios, A., Rappel, W. J., Acebron, J., Baglio, S. & Ando, B. [2004] "Emergent oscillations in unidirectionally coupled overdamped bistable systems," *Phys. Rev. E* **70**, 036103-1–12.

Chickarmane, V., Troein, C., Nuber, U. A., Sauro, H. M. & Peterson, C. [2006] "Transcriptional dynamics of the embryonic stem cell switch," *PLoS Comput. Biol.* **2**, e123.

Cohen, M. A. & Grossberg, S. [1983] "Absolute stability of global pattern formation and parallel memory storage by competitive neural networks," *IEEE Trans. Syst. Man Cybern.* **13**, 815–826.

Dellnitz, M. & Hohmann, A. [1997] "A subdivision algorithm for the computation of unstable manifolds and global attractors," *Numer. Math.* **75**, 293–317.

Doedel, E., Keller, H. B. & Kernevez, J. P. [1991a] "Numerical analysis and control of bifurcation problems: I," *Int. J. Bifurcation and Chaos* **1**, 493–520.

Doedel, E., Keller, H. B. & Kernevez, J. P. [1991b] "Numerical analysis and control of bifurcation problems: II," *Int. J. Bifurcation and Chaos* **1**, 745–772.

Doedel, E. & Wang, X. [1994] *Auto94*: *Software for Continuation and Bifurcation Problems in Ordinary Differential Equations*, Applied Mathematics Report, California Institute of Technology.

Doedel, E. [2010] *Lecture Notes on Numerical Analysis of Nonlinear Equations*, http://cmvl.cs.concordia.ca/auto/notes.pdf, pp. 189–196.

Ermentrout, B. [2002] *Simulating, Analyzing, and Animating Dynamical Systems*: *A Guide to XPPAUT for Researchers and Students* (SIAM).

Gardner, T. S., Cantor, C. R. & Collins, J. J. [2000] "Construction of a genetic toggle switch in *Escherichia coli*," *Nature* **403**, 339–342.

Goldbeter, A. & Koshland, D. E. Jr. [1981] "An amplified sensitivity arising from covalent modification in biological systems," *Proc. Natl. Acad. Sci. USA* **78**, 6840–6844.

Guckenheimer, J. & Vladimirsky, A. [2004] "A fast method for approximating invariant manifolds," *SIAM J. Appl. Dyn. Syst.* **3**, 232–260.

Henderson, M. E. [2003] "Computing invariant manifolds by integrating fat trajectories," *SIAM J. Appl. Dyn. Syst.* **4**, 832–882.

Hoffmann, M., Kopka, P. & Voges, E. [1999] "All-silicon bistable micromechanical fiber switch based on advanced bulk micromachining," *J. Select. Topics Quant. Electron.* **5**, 46–51.

Hopfield, J. J. [1982] "Neural networks and physical systems with emergent collective computational abilities," *Proc. Natl. Acad. Sci. USA* **79**, 2554–2558.

Hopfield, J. J. [1984] "Neurons with graded response have collective computational properties like those of two-state neurons," *Proc. Natl. Acad. Sci. USA* **81**, 3088–3092.

In, V., Bulsara, A., Palacios, A., Longhini, P., Kho, A. & Neff, J. [2003] "Coupling-induced oscillations in overdamped bistable systems," *Phys. Rev. E* (*Rapid Comm.*) **68**, 045102-1.

Krauskopf, B. & Osinga, H. [1999] "Two-dimensional global manifolds of vector fields," *Chaos* **9**, 768–774.

Krauskopf, B., Osinga, H. M., Doedel, E. J., Henderson, M. E., Guckenheimer, J., Vladimirsky, A., Dellnitz, M. & Junge, O. [2005] "A survey of methods for computing (un)stable manifolds of vector fields," *Int. J. Bifurcation and Chaos* **15**, 763–791.

Lyons, D., Mahaffy, J. M., Palacios, A., In, V., Longhini, P. & Kho, A. [2010] "Basins of attraction in a ring of overdamped bistable systems with delayed coupling," *Phys. Lett. A* **374**, 2709–2722.

Lyons, D., Mahaffy, J. M., Wang, S., Palacios, A. & In, V. [2014] "Computer code for the computational and visualization of basins of attraction," http://www.rohan.sdsu.edu/~antoniop/research/CCFM_manifolds/CCFM_manifolds.html.

Qiu, J. & Lang, J. H. [2004] "A curved-beam bistable mechanism," *J. Microelectromech. Syst.* **13**, 137–146.

Schmitt, O. H. [1938] "A thermionic trigger," *J. Scient. Instrum.* **15**, 24–26.

Solomon, M. J. [2003] "Hysteresis meets the cell cycle," *Proc. Natl. Acad. Sci. USA* **100**, 771–772.

Teschl, G. [2012] *Ordinary Differential Equations and Dynamical Systems*, Vol. 40 (Amer. Math. Soc.).

Tome, T. & De Oliveira, M. [1990] "Dynamic phase transition in the kinetic Ising model under a time-dependent oscillating field," *Phys. Rev. A* **41**, 4251–4254.

Tyson, J. J., Chen, K. & Novak, B. [2001] "Network dynamics and cell physiology," *Nat. Rev. Molecul. Cell Biol.* **2**, 908–916.

Voigt, C. A., Wolf, D. M. & Arkin, A. P. [2005] "The *Bacillus subtilis sin* operon," *Genetics* **169**, 1187–1202.

Wiggins, S. [1990] *Introduction to Applied Nonlinear Dynamical Systems and Chaos* (Springer-Verlag).

Wilhelm, T. [2009] "The smallest chemical reaction system with bistability," *BMC Syst. Biol.* **3**, 90–98.

Appendix A

Methods Parameters Computing 1D Stable Manifolds for Saddle Points

The 1D stable manifolds described in this paper were obtained via time-reversed numerical integration as described in the Methods section of the paper. The numerical parameters used are given in Table 1.

Table 1. Parameters for computing 1D stable manifolds. Each of the M 1D stable manifolds is obtained by numerically integrating from the two initial conditions $\mathbf{x}_\pm = \mathbf{x_e} \pm \delta\mathbf{v}$, where $\mathbf{x_e}$ is the saddle point. Numerical integration is from t_i to t_f with data saved every h. Note that $\mathbf{v}$ is an eigenvector along the 1D linear stable manifold at the saddle point.

λ	M	$t_i : h : t_f$	δ
−1.200	1	0:−0.005:−100	$0.001/\lvert\mathbf{v}\rvert$
−0.5500	2	0:−0.005:−100	$0.001/\lvert\mathbf{v}\rvert$
−0.4400	6	0:−0.005:−15	$0.005/\lvert\mathbf{v}\rvert$
−0.4300	6	0:−0.005:−15	$0.001/\lvert\mathbf{v}\rvert$
0	6	0:−0.005:−15	$0.001/\lvert\mathbf{v}\rvert$
0.4345	6	0:−0.005:−15	$0.001/\lvert\mathbf{v}\rvert$
0.4348	6	0:−0.005:−15	$0.001/\lvert\mathbf{v}\rvert$

Computing 2D Stable Manifolds for Saddle Points

Each 2D stable manifold is obtained via time-reversed numerical integration of a locus of P points lying in the 2D linear stable manifold of the saddle point $\mathbf{x_e} = (x_{e,1}, x_{e,2}, x_{e,3})$. The P points are selected by the following criteria: Let $\mathbf{v_1} = (v_{11}, v_{12}, v_{13})$ and $\mathbf{v_2} = (v_{21}, v_{22}, v_{23})$ be the two eigenvectors that span the 2D linear stable manifold at $\mathbf{x_e}$. Let $r \ll 1$ and $\theta_i = 2\pi i/P$. Then the points on the locus are given by:

$$x_{1,i} = r\cos(\theta_i)v_{11} + r\sin(\theta_i)v_{12} + x_{e,1}$$

$$x_{2,i} = r\cos(\theta_i)v_{21} + r\sin(\theta_i)v_{22} + x_{e,2}$$

$$x_{3,i} = r\cos(\theta_i)v_{31} + r\sin(\theta_i)v_{32} + x_{e,3},$$

for $i = 0, 1, \ldots, P-1$. Many points are saved from the numerical integration, as listed in Table 2.

Table 2. Parameters for computing 2D stable manifolds. Each of the M 2D stable manifolds is obtained by numerically integrating from a locus of P initial conditions $(x_{1,i}, x_{2,i}, x_{3,i})$ where $\mathbf{x_e}$ is the saddle point. Numerical integration is from t_i to t_f with data saved every h. Note that $\mathbf{v}$ is the eigenvector along the 1D linear stable manifold at the saddle point. The parameter `norm_tol` is set to 0.01 for all surfaces.

λ	M	$t_i : h : t_f$	r	P
−0.4400	6	0:−0.25:−25	0.05	401
−0.4300	6	0:−0.1:−25	0.01	201
−0.4300	6	0:−0.1:−25	0.1	201
0	12	0:−0.1:−25	0.01	201
0.4345	6	0:−0.1:−25	0.1	401
0.4345	6	0:−0.1:−25	0.1	201
0.4348	6	0:−0.1:−25	0.1	201
2.0000	1	0:−0.25:−60	0.05	201

Since each 2D stable manifold is bounded by two 1D stable manifolds, the points obtained from numerical integration for each 1D stable manifold are saved with the points for computing the corresponding 2D stable manifold to compute a better surface. To reduce the number of saved points, many points are removed so that the minimum distance between points is `norm_tol`. The function `Delaunay_special_plot` is called to perform surface triangulation with the 2D stable manifold points. This function first calls the open source function `Delaunay2_5D` to perform surface triangulation and outputs the indices of the triangles in a three column matrix. `Delaunay_special_plot` then calls `tri_calc` to count the number of inside triangles, boundary triangles, and outside triangles. We define an inside triangle as a triangle with all three triangle vertices satisfying

$$|x_i| < \texttt{cut\_val} \tag{A.1}$$

with `cut_val` = 1.5, for each $i = 1, 2, 3$. We define a boundary triangle as a triangle with only one or two vertices that satisfy Eq. (A.1), while an outside triangle sees all three vertices fail to satisfy Eq. (A.1). The outside triangles are discarded and the inside triangles are saved, but the boundary triangles are remade so that the surface to be constructed extends smoothly to the boundary prescribed by `cut_val`, which is accomplished by calling the function `polydraw`. Each boundary triangle has exactly one or two vertices that satisfy Eq. (A.1). For each triangle with exactly one vertex satisfying Eq. (A.1), there are two vertices that do not satisfy Eq. (A.1). As described in Fig. 15, linear interpolation is done between each outside vertex and the single inside vertex to obtain two new triangle vertices, each with one component equal to `cut_val` so that a new triangle is formed in the same plane as the previous boundary triangle. For the second case with two inside vertices and one outside vertex, three new triangles are formed in the same plane as the boundary triangle, as shown in Fig. 15.

After `polydraw` is called, all of the inside triangles and the triangles obtained from `polydraw` are saved into a single three column matrix containing indices of these triangles. The 2D stable manifold surface is then plotted with the plotting function `tri_surf`. The reader may refer to the function listing of `Delaunay_special_plot`, where the color and transparency properties of the 2D stable manifold surface are altered and the triangle edges are

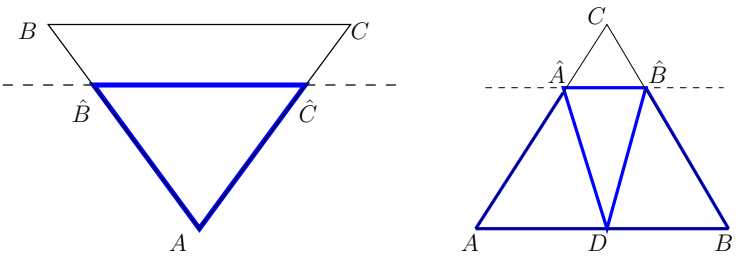

Fig. 15. (a) Two outside vertices: Linear interpolation is used to create a new triangle $A\hat{B}\hat{C}$ in the same plane as the boundary triangle ABC and (b) one outside vertex: Three new triangles, i.e. $A\hat{A}D$, $D\hat{A}\hat{B}$, and $BD\hat{B}$, replace the boundary triangle ABC, with two new points, $\hat{A}$ and $\hat{B}$ obtained on the boundary via linear interpolation, and the midpoint D of the two inside vertices is the third new point.

removed. All 2D stable manifolds are by default colored green and for images with 12 2D stable manifolds, 6 of them are colored lavender manually using the MatLab Property Editor GUI and setting the RGB value of the Patch Face property of each surface to $[0.85, 0.7, 1]$, i.e. lavender.

Computing 2D Stable Manifolds for Unstable Limit Cycles

This section describes the procedure for computing the 2D stable manifolds of unstable limit cycles arising from two subcritical Hopf bifurcations. As described above, the unstable limit cycle orbits were obtained from XPPAUT in AUTO and directly imported into MatLab. To run XPPAUT, the differential equations, system parameters, and numerical parameters must be written to a .ode file. After starting XPPAUT, forward numerical integration is used to obtain a stable equilibrium point. AUTO may then be opened from within XPPAUT. Numerical continuation of branches of equilibria is done in AUTO to obtain the three synchronous equilibria. Hopf bifurcations are located on the synchronous equilibria and are "grabbed" within AUTO to perform numerical continuation of the corresponding unstable periodic orbit. An unstable periodic orbit is then grabbed with AUTO. The user should next return to the main window of XPPAUT to "freeze" the graph of the orbit and export the data for each state variable as a .dat file. The data for each state variable may be easily combined into a single .txt or .xls file and imported as a matrix into MatLab.

From XPPAUT, 61 points were obtained for the limit cycle at each λ value. Let $l_{i,j}$ represent the x_i coordinate of the jth limit cycle point, where $i = 1, 2, 3$, and $j = 1, \ldots, \texttt{points}$. Numerical parameters `step` and Δx were chosen for numerical integration. Let $l_{j,\min} = l_{i,j} - \Delta x$. The allowed choices for x_1, x_2, x_3 are obtained from the following:

$$x_1 \in \left\{ l_{1,\min}, l_{1,\min} + \texttt{step}, \ldots, l_{1,\min} + \frac{2\Delta x}{\texttt{step}} \right\}$$

$$x_2 \in \left\{ l_{2,\min}, l_{2,\min} + \texttt{step}, \ldots, l_{2,\min} + \frac{2\Delta x}{\texttt{step}} \right\}$$

$$x_3 \in \left\{ l_{3,\min}, l_{3,\min} + \texttt{step}, \ldots, l_{3,\min} + \frac{2\Delta x}{\texttt{step}} \right\}.$$

Note that there are $P = 2\Delta x/\texttt{step} + 1$ possible choices for each x_1, x_2, and x_3, so there are P^3 distinct initial conditions that correspond to the jth limit cycle point with coordinates $(l_{1,j}, l_{2,j}, l_{3,j})$, so that in total, the number of initial conditions used is $P \times \texttt{points}$. Note that for all of the λ values listed in the table, $P = 3$ and $\texttt{points} = 61$, so that $P^3\texttt{points} = 3^3 \times 61 = 1647$ total initial conditions were used for a given λ value. Though the numerical parameters `step` and Δx are the same in the table for each entry, `step` may be decreased to obtain a higher quality surface.

Time-reversed numerical integration of the set of initial conditions was used to obtain points on the 2D stable manifold. Many points were saved at select nodes. At this point, the same procedure was used for surface triangulation and graphing as

Table 3. Parameters used for computing the 2D stable manifolds of the unstable limit cycles arising from subcritical Hopf bifurcations. The parameter `norm_tol` is set to 0.01 for all surfaces.

λ	Step	Δx	$t_i : h : t_f$	`Points`
−0.4681	0.001	0.001	0:−0.25:−30	61
0.4592	0.001	0.001	0:−0.25:−30	61

described in the section above for 2D stable manifolds of saddle points. The parameters used are listed in Table 3.

Appendix B
Code Listing

The purpose of this Appendix is to briefly describe the MatLab code used for producing the figures in this paper. A list of main driver programs is given in the next subsection. Each driver program corresponds to a particular interval of the parameter λ. Hence, to reproduce a specific figure, one should locate the driver program relevant to the corresponding λ value, and see the brief instructions given for running that program. Following the driver program section is a brief summary of the two functions used to compute the 2D stable manifolds.

Main Driver Programs

The following is a list of main driver programs used for producing many of the figures in this paper. It is located in the directory `.../CCFM_manifolds/driver/`. Note that the file path variable called `mypath` at the beginning of each driver program must be updated by the user to the local directory containing the folder `CCFM_manifolds` so that the definitions of the MatLab functions to be called may be found by MatLab when executing the script.

`CCFM_bif_diagram.m`: Bifurcation Diagram (Fig. 1)

This program computes the main bifurcation diagram for the CCFM system. Beginning at $\lambda = -0.43$, this program computes 27 branches of equilibria, where they exist, by proceeding toward negative λ to $\lambda = -3$. Then the program goes back to $\lambda = -0.43$ and increases λ by small increments until $\lambda = 3$. The function `branch_plot` is called to compute and plot the stability according to the color of each equilibrium branch. For each λ value, this function calls `compute_fixed_points` to numerically solve a nonlinear system of equations to obtain the fixed points. If the branch is nonexistent for this λ-value, the value of the fixed point is returned as `NaN` and will not be plotted later. The MatLab command prompt may print an error message when `compute_fixed_points` cannot compute a fixed point at a particular λ value. This is an indication that it can no longer follow the current branch. Next, `branch_plot` calls the function `CCFM_Jac`, which computes the Jacobian matrix, and `stability_info` returns the eigenvalues of the Jacobian matrix and a scalar `type` according to the type of equilibrium point. The branch point is plotted by color according to `type`. See the program `CCFM_bif_diagram.m` for further details.

`manifold_1D_stable.m`: $\lambda < -0.5018$ [Figs. 2, 4(a)]

This program works for two λ regimes. The first regime is $\lambda < -0.6667$. In this λ range, the origin is the only equilibrium point with a 1D stable manifold. It may be computed with the parameters described in Table 1. For the second regime, i.e. $-0.6667 < \lambda < -0.5018$, there are two synchronous equilibria with 1D stable manifolds. Note that the parameter λ is set by setting `lambda_min` on line 86. No other changes are needed to run this driver file.

`unstable_hopf_2D_manifold.m`: $-0.5018 < \lambda < -0.4475$ and $0.4349 < \lambda < 1.3333$ [Figs. 4(b), 9(b)]

The program computes the 2D stable manifold for the unstable limit cycle emanating from a subcritical Hopf bifurcation. Parameters that may be used are given in Table 3. Although the parameters are only listed for a few values of λ, the 2D stable manifold for the unstable limit cycle for other values of λ may be computed, as many more were imported from AUTO in XPPAUT. As with the previous section, this program works with two parameter regimes. The first parameter regime is $-0.5018 < \lambda < -0.4475$ and the second parameter regime is $0.4349 < \lambda < 1.3333$. Along with using the parameters listed in Table 3, the user must input the desired λ value and filename of the unstable limit cycle orbit on lines 51–52.

`stablemanifold_two_basins_lambda_44.m`: $-0.4475 < \lambda < -0.4346$ (Fig. 5)

This driver program is used to compute the six 1D stable manifolds and the six 2D stable manifolds of saddle points, with numerical parameters listed in Tables 1 and 2, over the range $-0.4475 < \lambda < -0.4346$. The λ parameter is controlled here by setting the value of `lambda_min` on line 145.

`stablemanifold_eight_basins.m`:
$-0.4346 < \lambda < 0.4346$ [Figs. 6(a), 7, 8(a)]

This driver program is used to compute the six 1D stable manifolds and 12 2D stable manifolds of saddle points, with numerical parameters listed in Tables 1 and 2, over the range $-0.4346 < \lambda < 0.4346$. The parameter λ is controlled by setting the variable `lambda_val` on line 19. Note: To generate the figure with $\lambda = 0$, `lambda_val` should be set to -0.001 or 0.001, since the 2D stable manifolds cannot be directly generated with $\lambda = 0$.

`stablemanifold_two_basins_lambda_4348.m`:
$0.4346 < \lambda < 0.4349$ [Fig. 9(a)]

This driver program is used to compute six 1D stable manifolds and six 2D stable manifolds of saddle points, with numerical parameters listed in Tables 1 and 2. The parameter λ may be varied within the range $0.4346 < \lambda < 0.4349$, but the program is ready to run for $\lambda = 0.4348$. To change the value of λ, the variable `lambda_max` should be changed on line 115. No commenting or uncommenting of code is needed to run this program.

`basins_stablemanifold.m`: $1.3333 < \lambda$ (Fig. 10)

This driver program is used to compute the 2D stable manifold of the origin for $\lambda > 1.3333$, with numerical parameters listed in Table 2. Note that λ may be changed by changing the variable `lambda` on line 17, and the program is ready to run with no further alterations needed by the user.

Stable Manifold Computation Programs

The directory `.../CCFM_manifolds/functions/` contains the functions called by the driver programs. Many of the functions called are described briefly in Appendix A where relevant. The two functions called by the main driver programs to compute 2D stable manifolds are briefly summarized below.

`manifold_compute_circle.m`

This function computes the 2D stable manifold of a corresponding saddle point by taking a locus of points in the 2D stable linear eigenspace of the saddle point, numerically integrating in reverse time using the MatLab integrator `ode23`, and saving a large number of points for surface triangulation. Recall that this locus of initial conditions is described above in Appendix A.

`manifold_compute_ulc.m`

This function computes the 2D stable manifold of the unstable limit cycle arising from a Hopf bifurcation by taking a set of initial conditions described above in Appendix A, numerically integrating in reverse time using the MatLab integrator `ode23`, and saving a large number of points for surface triangulation.